Single-molecule switching via controlled tautomerization at room temperature

Wenjing Hong (whong@xmu.edu.cn)
Xiamen University https://orcid.org/0000-0003-4080-6175

Chun Tang
Xiamen University

Thijs Stuyver
The Hebrew University

Yiling Ye
Xiamen University

Jun-yang Liu
Xiamen University

Jia Shi
Xiamen University

Sason Shaik
The Hebrew University

Haiping Xia
Southern University of Science and Technology

Physical Sciences - Article

Keywords: nanodevices, tautomerization, switching mechanism, switching devices

Posted Date: October 21st, 2020

DOI: https://doi.org/10.21203/rs.3.rs-92090/v1

Abstract

The control of chemical reactivity at the single-molecule scale offers a unique opportunity for the design and fabrication of advanced nanodevices.1-3 As a prototypical reaction, tautomerization has been extensively explored as a promising tool for manipulating the single-molecule conductance of tetrapyrrole macrocycles absorbed on a surface.4-8 However, the resulting molecular devices were determined to undergo dynamic, spontaneous interconversions even under cryogenic conditions, so that control of tautomeric switching between well-defined and specific states remains challenging. Here, we report the design of a reversible single-molecule switch based on an enol-keto tautomerization reaction, which demonstrates controllable bistability and inhibits spontaneous interconversion even at room temperature. Such control is achieved by modulating the potential energy surface (PES) through a bias-triggered charge injection process. Our results reveal that the device operates through switching between two distinct redox-related PESs with opposite thermodynamic driving forces, i.e., one exhibits strong preference for the conducting enol form, while the other exhibits a preference for the insulating keto form. The described switching mechanism constitutes a promising approach to achieve robust switching devices at the single-molecule scale.

Main Text

The ability to modulate the electrical signal passing through devices by switching between two or more well-defined states is essential for the design of logical circuits in data storage and processing.[9] Control of chemical reactions via inherent electronic triggers offers a promising switching mechanism at the single-molecule scale, thus opening an avenue for molecular-scale devices with bistability.[2] As a ubiquitous type of intramolecular chemical reaction, tautomerization is an ideal *mode of operation* to realize such a single-molecule switch with bistability. Over the past decade, tautomerization has been demonstrated in the surface-based characterization of tetrapyrrole macrocycles, such as porphyrins and naphthalocyanine[4-6,10,11] using scanning tunnelling microscopy (STM) and atomic force microscopy (AFM). Although distinct states have been observed for these macrocycles upon their absorption on flat surfaces, the resulting pairs of tautomeric states are generally degenerate or quasi-degenerate with a low isomerization barrier[12]. Due to the low barrier, the interconversion between the tautomeric states is in dynamic balance and spontaneously occurs even under cryogenic conditions, which prevents the potential application of the single-molecule tautomerization in the construction of controllable molecular devices. Furthermore, the in-plane charge transport through the surface-based devices limits the maximal conductance difference between the tautomeric states, and the highest switching ratio is still below ~300%.[4,5]

Here, we report the reversible switching between two tautomeric states at the single-molecule scale with controlled bistability operated by a moderate bias at room temperature. The mode of operation in our switching device involves two redox-related PESs, one corresponding to the uncharged ground state of the molecular bridge (MB; Fig. 1a, upper panel), and the other one corresponding to a positively charged

state of the MB (Fig. 1a, lower panel). On the first PES (PES *I*, Fig. 1a), the keto form is the thermodynamically stable form with a relatively high barrier associated with an energetically unfavorable four-membered cyclic transition state (Fig. 1a),[13] which suppresses any further dynamic and thermal interconversion. Upon charge injection, the second PES becomes accessible (PES *II*, Fig. 1a) with dramatically reduced tautomerization barrier and reversed thermodynamic driving force. Consequently, the keto form is readily converted into the enol form on the resulting PES *II*, until an electron is injected back into the MB from one of the contacts. The molecular devices are characterized by the scanning tunnelling microscope break junction (STM-BJ) technique[14,15] (Fig. 1b). By adjusting the bias, the charge injection can be reversibly manipulated, and the conductance difference between the switching states of the keto (s bridge) and enol form (p bridge) reaches ~6700%.

To ensure that the charge transport pathway passes through the tautomerization unit, we designed molecule **A** with the keto-enol unit (red parts in Fig. 2a) between two thioanisole anchors (blue parts in Fig. 2a). The anchors facilitate the connection of the molecular components to the gold electrodes. Molecule **A** can be synthesized at the gram scale by an electrophilic substitution reaction in one step (see details in the Methods Section). From the NMR characterization of the resulting compound (Extended Data Fig. S7), we observe the exclusive presence of keto form **A** (Fig. 2a), indicating that this form dominates the tautomeric equilibrium. In the structure of **A**, the methylene group blocks the conjugation between the phenyl groups of the thioanisole anchor units. Thus, **A** is expected to exhibit a significantly lower conductivity in the sulfur-to-sulfur pathway than its corresponding tautomeric isomer **B**, i.e., the isomer with a p-bridge between the two phenyl groups. Such an enol form can also be trapped by methylation, leading to molecule **B-OMe** as a reference (Fig. 2a).

To investigate the charge transport through single-molecule junctions of **A**, we dissolved 0.1 mM **A** in 1,2,4-trichlorobenzene solvent and characterized the resulting solution by STM-BJ experiments at room temperature. As shown in Fig. 2e, the individual conductance traces (conductance vs. stretching distance) characterized at a 0.1 V bias show conductance plateaus (blue traces) between 10^{-4} and 10^{-5} G_0 (G_0 is the quantum conductance, where G_0 = 77.6 mS).[16] After increasing the bias to a moderate 0.6 V, we observe another conductance plateau with a higher conductance located between 10^{-2} and 10^{-3} G_0 (red traces). By overlapping more than 3000 such conductance traces, we obtain the two-dimensional (2D) conductance histograms shown in Fig. 2b and 2c (cf. Extended Data Fig. 3 for 2D histograms at intermediate bias voltages). These 2D histograms show similar shapes of conductance plateaus in distinct conductance ranges. We further analyze the stretching distance distributions of the conductance plateaus. As shown in the inset of Fig. 2b and Fig. 2c, the stretching distances of the conductance plateaus are similar at 0.1 and 0.6 V biases. After considering a 0.5 nm snap-back distance after the breaking of the gold-gold atomic contact,[17] the calibrated length of the molecular junctions at 0.1 and 0.6 V biases correspond to 0.92 and 0.95 nm, respectively. The consistency of these stretching distances associated with the molecular length suggests that a robust sulfur-to-sulfur charge transport pathway remains intact at different bias voltages.

One-dimensional (1D) conductance histograms were constructed from more than three thousand traces without data selection at different bias voltages up to 0.6 V. As shown in Fig. 2d, the peak center (determined by Gaussian fitting) of the 1D conductance histograms at 0.6 V is located at $10^{-2.82}$ G_0, which is ~6700% fold to the conductance at 0.1 V ($10^{-4.65}$ G_0). The 1D conductance histograms at biases ranging from 0.1 to 0.3 V are all very similar, showing an approximately invariant single conductance peak centered around $10^{-4.6}$ G_0, which we defined as the low-conductance state and labeled '**L**'. Increasing the bias beyond 0.4 V, we observe a double peak distribution, with a new peak gradually emerging at around $10^{-2.8}$ G_0, which we defined as the high-conductance state and labeled '**H**'. The '**H**' state becomes increasingly prominent as the bias increases and starts to dominate at the bias voltage of 0.6 V. This dramatic conductance switching suggests that the applied bias effectively transforms the nonconductive **A** to a highly conductive state similar to **B**. To confirm the transformation, a stabilized enol form of **B**, **B-OMe** (Fig. 2a), was characterized at 0.1 V, and the resulting single conductance peak is centered at $10^{-3.06}$ G_0 (Fig. 2d). Increasing the bias up to 0.6 V does not discernably change the location of this peak (Extended Data Fig. 4). The similarity in the conductance characteristics for **B-OMe** and the '**H**' state suggests that the emergence of the '**H**' state at high bias is associated with a conversion from the keto form to the enol form. Owing to a high barrier in the neutral PES (*vide infra*), we propose the '**H**' state is the (positively) charged enol form of **B**, which can be reached thermally on the charged PES.

Through analysis of the probabilities of the occurrence of the '**H**' and '**L**' states at different bias voltages, we constructed the scatter diagram shown in Fig. 2f. The probability of the '**H**' state begins to rise when the bias exceeds 0.4 V, while the probability of the '**L**' state decreases significantly. The two probabilities become almost equal at 0.6 V bias. At a 0.7 V bias, the probability of the '**H**' state further increases to 67%. At voltages exceeding 0.7 V, the formed single-molecule junctions become increasingly unstable, which renders characterization of the corresponding probabilities unfeasible. More importantly, we find that the switching between the '**H**' and '**L**' states is reversible. To assert this, we switched the bias voltages between 0.1 and 0.6 V in an alternating fashion. We collected approximately one thousand conductance traces for three subsequent cycles to determine the most-probable conductance (Extended Data Fig. 5), as shown in Fig. 2g, which demonstrates robust and reversible switching of the single-molecule conductance.

To further reveal the switching between the '**H**' and '**L**' states, we also recorded the evolution of the current as a function of continuously varied bias for individual junctions. During the break junction process with a 0.1 V bias applied, once we observed a conductance plateau formed between 10^{-4} and 10^{-5} G_0, the movement of the gold tip was halted, and a bias voltage ranging from -1 to 1 V was scanned (further details are described in the Methods section)[18]. As shown in Fig. 3a, the so-recorded *I-V* curves (831 out of 13850 traces) exhibit clear current switching as the bias voltage increases (the other traces exhibit a regular proportional increase in the current with increasing bias). Four representative *I-V* traces exhibiting this "jumping behavior" are plotted in the 2D *I-V* histogram shown in Fig. 3a. The sudden nature of the current jump suggests an abrupt electronic transition occurring on the MB.

We further applied transition voltage spectroscopy (TVS)[19,20] to gauge the alignment between the Fermi energy of the electrodes and the main eigenchannel, i.e., the transport channel of the molecular junctions, which is the HOMO for molecule **A**. We selected a number of *I-V* curves (2542 traces from 3234 traces in Extended Data Fig. 6) not exhibiting the current jump and transformed the most representative *I-V* curve (yellow line in Fig. 3b) into a TVS spectrum (as shown in Fig. 3c). The resulting spectrum exhibits a minimum, which is called the transition voltage, at a bias of approximately 0.8 V, suggesting that the energy difference between the Fermi level of the electrodes and this transport channel amounts to approximately 0.4 eV. The magnitude of the spacing between the unbiased Fermi level (E_F) and the HOMO channel is in line with the observed robustness of the '**L**' state in Fig. 2d up to a moderate voltage; the transport regime within this entire bias window, i.e., [E_F - eV/2, E_F + eV/2], is entirely off-resonant so that the transmission probability of incoming electrons through the MB (and thus the conductance) remains approximately constant, irrespective of the considered bias voltage. This is a clear indication that the sudden emergence of the '**H**' state at voltages exceeding 0.4 V is caused by a structural modification of the MB.

To further elucidate the switching mechanism, we performed DFT calculations on a model system consisting of the bare molecule **A** in the absence of Au clusters and thiomethyl-groups (Fig. 4a; cf. Section S2 of the Supporting Information for an in-depth discussion of the effect of the anchor groups). First, the PES associated with the neutral species was considered. In accordance with the experimental observations, we observe that at the B3LYP/def2-TZVP level of theory (full computational details can be found in the Methods Section), the enol form lies 7.5 kcal mol^{-1} higher in energy than the keto form. This energy difference persists even in the presence of an electric field corresponding to the field exerted by the approximate threshold voltage for switching in the junction (F_Z = + 0.05 V/Å; cf. Fig. 4a). This finding constitutes an unequivocal confirmation that tautomeric interconversion cannot occur on the (uncharged) ground-state PES (in blue): even if a kinetically accessible reaction pathway connecting the keto and enol form could be identified, the population of the enol form would always remain negligible at room temperature.

Concerning the kinetics of the tautomeric interconversion process, our calculations indicate that the barrier separating the keto and enol forms is unsurmountable; the direct tautomerization mechanism, i.e., the H-atom shuttling from the carbon to the oxygen center (Fig. 4a), corresponds to a potential energy hill of 60.1 kcal mol^{-1}. With the help of a control experiment in the glovebox (Extended Data Fig. 2a), which enabled control over the presence of trace amounts of H_2O, we could rule out any alternative water-assisted tautomerization mechanism (Extended Data Fig. 2b-e and Fig. 9).[21-23] The isotope effect is also proven to be very weak (Extended Data Fig. 1), which rules out a proton tunnelling mechanism. Meanwhile, no other source of acids or bases is present in the reaction medium to catalyze the process, assuming that the enol form is thermodynamically and kinetically inaccessible on the ground-state PES is reasonable. Furthermore, since the experiment is performed in the absence of a light source, any mechanism involving a transition – upon absorption of a photon – to the PES of an (equally uncharged) excited state can also be ruled out.[24-26]

Our calculations suggest that removing an electron from the neutral model system dramatically impacts the kinetics and thermodynamics associated with the keto-enol tautomerization. In the positively charged system (Fig. 4a in red), the enol form becomes the thermodynamically stable form, with a driving force of 22.0 kcal mol^{-1}. This thermodynamic reversal from keto to enol preference upon oxidation of tautomeric compounds is well documented in the literature.[27-30] Associated with the switch in the thermodynamic preference, the energy hill separating both states is remarkably reduced upon removal of an electron: the barrier associated with this reaction pathway decreases to 22.9 kcal mol^{-1} for the cationic species (Fig. 4a), which can be readily crossed at room temperature. The root cause of the dramatic change in the reaction profile upon charge injection is straightforwardly revealed by a qualitative valence bond analysis (cf. Section S3 in the Supporting Information). Thus, our computational analysis suggests that only a redox-based mechanism is viable for the tautomerization of the MB. Calculating the transmission spectra for the candidate OFF and ON state associated with this proposed switching mechanism (cf. Fig. 4c), i.e., the uncharged keto-species and the positively charged enol-species respectively, leads to a conductance ratio in the transmission spectrum region corresponding to the bias window that is qualitatively in line with the experimentally obtained value (~ 100:1), which further strengthens this hypothesis.

At this point, it is important to note that our experimental results indicate that the charging event does not require a crossing between the chemical potential of one of the contacts and the transport channel associated with the HOMO of the MB (cf. the TVS in Fig. 3c), in contrast to what could be expected from a pure Landauer-Büttiker framework. Fig. 2f also indicates that there is no fixed threshold bias triggering the switch; beyond a bias of 0.4 V, the proportion of '**H**' traces gradually increases. This realization suggests that the charge injection that triggers the tautomerization reaction is a thermal transition (cf. Marcus theory of electron transfer[31]): as the chemical potential of (one of) the contacts is lowered through the application of the bias, the thermal barrier for the charge transfer process can be expected to decrease gradually, which concomitantly increases the probability of such an event occurring (Fig. 4b; cf. Section S4 in the Supporting Information). As soon as the PES of the charged species is reached through this thermal transition, the associated thermodynamic driving force will steer the MB from its insulating keto form to conducting enol form, and hence the observed conductance switching is obtained. Note that this finding of the role of the molecular states in the transport properties of the junction underscores the intimate relationship and interplay between the Landauer-Büttiker and Marcus frameworks to describe molecular conductance.[32,33]

In summary, we presented a bias-triggered keto-enol tautomerization switch with controlled bistability in a single-molecule junction, and the switching can be reversibly operated between two defined states even at room temperature. The charge injection from the molecular bridge to the electrodes plays a pivotal role in modifying the PES, which leads to effective regulation of the tautomeric equilibrium. The switching between the two PESs controls both the thermodynamic driving forces and the kinetic barriers, ensuring

robust bistability of the resulting devices. The presented two-terminal device structure breaks the limitation of the previously considered surface-based devices, leading to a ~6700% conductance difference between the tautomeric states, which is more than one order of magnitude higher than the conductance difference previously obtained for in-plane molecular devices. Moreover, the functional unit of the molecular device is ubiquitous and can be straightforwardly synthesized, showing the potential to achieve robust, reversible, and scalable switching devices through the control of chemical reactivity at the single-molecule scale.

Methods

Conductance measurements

The single-molecule conductance was measured using the scanning tunnelling microscope break-junction (STM-BJ) technique with a home-built setup described previously.[34,35] A gold substrate was fabricated by depositing Cr/Au (10/100 nm) onto a silicon wafer with 300 nm silicon dioxide. The gold substrate was cleaned by piranha solution before the experiment. A gold tip was made by flame cleaning to form a gold bead. We circularly drove the gold tip in and out of contact with the gold substrate and continuously recorded the current signal with a fixed bias voltage. During the breaking of the gold-gold contact, a molecule may bridge the two *in-situ* formed electrodes, leading to a conductance plateau. We used a sampling rate of 20 kHz to collect more than 2000 traces to construct the conductance histograms.

State switching

The switching was performed by directly changing the bias voltage between 0.1 and 0.6 V. We collected approxmiately 1000 traces in each cycle step to construct the 1D conductance histograms. The peak center was determined by the Gaussian fitting. The error was defined as the standard deviation of the Gaussian fitting.

I-V characterization

The *I-V* characterization was modified from the previous protocol.[18,36] During the break junction process with a 0.1 V bias applied, once we observed a conductance plateaus formed between 10^{-4} and 10^{-5} G_0, we stopped the movement of the gold tip and scanned the bias voltage between -1 and 1 V. Before and after the voltage scan, we fixed the bias to 0.2 V and checked whether the measured conductance was still located between 10^{-4} and 10^{-5} G_0. We selected those *I-V* traces in which the conductance remained between 10^{-4} and 10^{-5} G_0 before and after the voltage scan. The 2D *I-V* histograms were plotted in a 200*200 array. We used Gaussian fitting for each column of the array to obtain the fitting line. The transition voltage spectrum was plotted from the above fitting line according to previous results.[20]

Determination of the probability of high- and low-conductance states

We used an auto-classification algorithm[37] based on spectral clustering to determine the ratio of the traces showing different conductance plateau values. When the bias is between 0.5 and 0.7 V, the conductance traces are clustered into two clusters, showing two clear molecular peaks located approximately $10^{-4.5}$ and $10^{-2.8}$ G_0 in the corresponding 1D conductance histograms. The probability is determined by the number of traces in one of the clusters over the total number of traces. When the bias is between 0.1 and 0.4 V, the number of high-conductance traces is low. We cluster the conductance traces into 5 clusters and take one of the clusters showing a clear conductance peak around $10^{-3.0}$ G_0 as the high-conductance state. We also remove the clusters that do not show conductance peak between $10^{-0.5}$ and $10^{-5.5}$ G_0. The residual clusters are determined to be the low-conductance state. The corresponding probabilities are determined by the number of high- or low-conductance traces over the total number of conductance traces.

Synthesis

1,2-Bis(4-(methylthio)phenyl)ethan-1-one **A**: To a solution of 2-(4-(methylthio)phenyl)acetic acid (10 mmol) in 50 mL dichloromethane, thionyl chloride (20 mmol) was added dropwise. A drop of dimethylformamide was also added to the solution. The reaction mixture was stirred for 1 h at room temperature. Then, the solvents were removed under vacuum. 2-(4-(Methylthio)phenyl)acetyl chloride was obtained in quantitative yield without further purification. Thioanisole (13 mmol) was dissolved in 25 mL dichloromethane at 0 ℃, and anhydrous aluminum chloride (13 mmol) was added slowly to the solution. Then, 2-(4-(methylthio)phenyl)acetyl chloride was added to the reaction mixture, and the solution was slowly heated to room temperature. After the (methylthio)phenyl)acetyl chloride was completely consumed, as detected by TLC, the reaction mixture was quenched with ice water. The organic phase was extracted by diethyl ether, which was collected and concentrated. The crude mixture was further purified by column chromatography to give **A**. Yield: 75%. White solid. ^{1}H NMR (500 MHz, $CDCl_3$): d = 7.90 (dt, *J* = 8.7, 2.0 Hz, 2H), 7.22 (m, 4H), 4.19 (s, -OC*H*$_3$, 3H), 2.51 (s, -SC*H*$_3$, 3H), and 2.46 (s, -SC*H*$_3$, 3H) ppm. ^{13}C NMR (125 MHz, $CDCl_3$): d = 196.52, 146.14, 136.94, 132.78, 131.53, 129.87, 129.03, 127.10, 125.04, 44.80, 15.99, and 14.74 ppm. HRMS (ESI): *m/z* calcd for $[C_{16}H_{16}NaOS_2]^+$, 311.05348; found, 311.0525.

1,2-Bis(4-(methylthio)phenyl)ethan-1-one-2,2-d2 **A-*d*$_2$**: To a solution of **A** (0.7 mmol) in CD_3OD (5 mL), 0.2 mL NaOD/D_2O solution (10%) was added. The reaction mixture was stirred for 1h at room temperature. Then, DCl was added dropwise until fully neutralized as detected by pH test strips. The organic phase was extracted by diethyl ether, and the crude mixture was purified by column chromatography to give **A-*d*$_2$**. Yield: 30%. While solid. ^{1}H NMR (500 MHz, $CDCl_3$): d = 7.90 (dt, *J* = 8.5, 1.8 Hz, 2H), 7.22 (m, 4H), 2.51 (s, -SC*H*$_3$, 3H), and 2.46 (s, -SC*H*$_3$, 3H) ppm. HRMS (ESI): *m/z* calcd for $[C_{16}H_{14}D_2NaOS_2]^+$, 313.06603; found, 313.0652.

(Z)-((1-methoxyethene-1,2-diyl)bis(4,1-phenylene))bis(methylsulfane) **B-OMe**: To a solution of **A** (0.7 mmol) in methanol (10 mL), trimethyl ester (0.85 mmol) and 4-toluenesulfonic acid (0.1 mmol) were

added. The reaction mixture was stirred at 60 °C for 12 h. Then, the reaction was quenched by an ammonium chloride solution. The crude mixture was extracted from diethyl ether and purified by column chromatography to give **B-OMe**. Yield: 35%. White solid. ^{1}H NMR (400 MHz, $CDCl_3$): d = 7.63 (d, *J* = 8.2 Hz, 2H), 7.47 (d, *J* = 8.2 Hz, 2H), 7.25 (m, 4H), 6.06 (s, 1H), 3.63 (s, -OCH_3, 3H), 2.52 (s, -SCH_3, 3H), and 2.50 (s, -SCH_3, 3H) ppm. ^{13}C NMR (100 MHz, $CDCl_3$): d = 155.61, 138.89, 136.43, 133.04, 132.91, 128.97, 126.81, 126.81, 126.62, 126.32, 111.90, 57.94, 15.92, and 15.64 ppm. See Supporting Information Section S1 for a more in-depth discussion and additional characterization spectra.

Theory

All geometry optimizations were performed at the B3LYP/def2-TZVP level with implicit inclusion of the apolar solvent through a PCM model in GAUSSIAN09.[38] Since the actual solvent used in the experiment, 1,2,4-trichlorobenzene (e = 2.25), is not available as a predefined solvent in GAUSSIAN09, the very similar tetrachloroethene (e = 2.5) was used instead. A small electric field of 0.05 V/Å – which corresponds approximately to the effective field experienced by the molecular bridge due to the switch-inducing bias applied between the two Au-contacts – was included in the calculations with the help of the "Field = M ± N" keyword (see Fig. 4 for the field direction; the GAUSSIAN convention was used here).[39,40] Due to the low field-strength and the low polarity of the solvent, one can expect the solvent screening to be negligible.[41] In the main text of the manuscript, we focused on F_Z = + 0.05 V/Å, but the molecule is equally likely to assemble between the two contacts in the opposite direction. Flipping the field, i.e. setting F_Z = - 0.05 V/Å, one obtains reaction barriers and thermodynamic driving forces that are consistently a couple of kcal/mol higher than the values reported in Fig. 4, cf., Extended Data Fig. 8.

Transport calculations

Transport calculations were performed using the non-equilibrium Green's function (NEGF) method combined with DFT as implemented in the Artaios code,[42] a post-processing tool for GAUSSIAN09. The electrode geometry used in this work consists of ten gold atoms per electrode, which are arranged as a six-atom triangular fcc-gold (111)-surface, together with a second layer consisting of three gold atoms, and finally an ad-atom on top. This ad-atom serves as the attachment point to the SMe anchor units. In line with the geometrical data from previous work,[43,44] the Au-S distance was set to 2.45 Å, the Me-S-Au angle was set to 100°, and the C(Ph)-S-Me angle was set to 110°. The dihedral angle between the S-Au bond and the plane of the adjacent phenyl groups was set to 0°, so that disproportionate through-space coupling contributions between the contacts in the latter junction could be avoided. For the resulting structures, single-point calculations were performed at the B3LYP/LanL2MB level of theory (a minimal basis set was chosen to avoid ghost transmission and excessive through-space coupling between the contacts), again using GAUSSIAN09 software.[45] In a final step, the Hamiltonian and overlap matrices were extracted to carry out the NEGF calculation within the wide-band-limit (WBL) approximation using the post-processing tool Artaios.[46] In the WBL approximation, a constant value of 0.036 eV^{-1} for the local density of states (LDOS) of the electrode surface was used. This value was taken from the literature.[46]

Declarations

Author contributions

T.C., X.H., and H.W. conceived the idea for the paper. T.C. synthesized and characterized the molecules under the supervision of X.H.. T.C. and Y.Y. conducted the conductance characterization under the supervision of H.W.. S.T. and S.S. conducted the theoretical calculations. T.C., S.T., S.S., X.H., and H.W. analyzed the data and wrote the paper with input from all the authors.

Acknowledgements

This work was supported by the National Key R&D Program of China (2017YFA0204902), the National Natural Science Foundation of China (Nos, 21673195, 21722305, 21703188, U1705254), and the Fundamental Research Funds for Xiamen University (20720190002). S. S. is supported by the Israel Science Foundation (ISF 520/18). T.S. acknowledges the Research Foundation-Flanders (FWO) for a position as postdoctoral research fellow (1203419N).

Competing interests The authors declare no competing interests

References

1. Aragonès, A. C. *et al.* Electrostatic catalysis of a Diels–Alder reaction. *Nature* **531**, 88-91 (2016).
2. Xiang, D., Wang, X., Jia, C., Lee, T. & Guo, X. Molecular-Scale Electronics: From Concept to Function. *Chem Rev* **116**, 4318-4440 (2016).
3. Su, T. A., Neupane, M., Steigerwald, M. L., Venkataraman, L. & Nuckolls, C. Chemical principles of single-molecule electronics. *Nat. Rev. Mater.* **1**, 16002 (2016).
4. Liljeroth, P., Repp, J. & Meyer, G. Current-Induced Hydrogen Tautomerization and Conductance Switching of Naphthalocyanine Molecules. *Science* **317**, 1203-1206 (2007).
5. Auwärter, W. *et al.* A surface-anchored molecular four-level conductance switch based on single proton transfer. *Nat. Nanotechnol.* **7**, 41-46 (2012).
6. Ladenthin, J. N. *et al.* Force-induced tautomerization in a single molecule. *Nat. Chem.* **8**, 935-940 (2016).
7. Fatayer, S. *et al.* Molecular structure elucidation with charge-state control. *Science* **365**, 142-145 (2019).
8. Doppagne, B. *et al.* Single-molecule tautomerization tracking through space- and time-resolved fluorescence spectroscopy. *Nat. Nanotechnol.* **15**, 207-211 (2020).
9. Li, H. B., Tebikachew, B. E., Wiberg, C., Moth-Poulsen, K. & Hihath, J. A Memristive Element Based on an Electrically Controlled Single-Molecule Reaction. *Angew. Chem. Int. Ed.* **59**, 11641-11646 (2020).

10. Iancu, V. & Hla, S.-W. Realization of a four-step molecular switch in scanning tunneling microscope manipulation of single chlorophyll-a molecules. *Proc. Natl. Acad. Sci.* **103**, 13718-13721 (2006).
11. Fatayer, S. *et al.* Reorganization energy upon charging a single molecule on an insulator measured by atomic force microscopy. *Nat. Nanotechnol.* **13**, 376-380 (2018).
12. Kügel, J., Sixta, A., Böhme, M., Krönlein, A. & Bode, M. Breaking Degeneracy of Tautomerization—Metastability from Days to Seconds. *ACS Nano* **10**, 11058-11065 (2016).
13. Shaik, S. S. & Hiberty, P. C. *A chemist's guide to valence bond theory*. (John Wiley & Sons, 2007).
14. Xu, B. & Tao, N. J. Measurement of single-molecule resistance by repeated formation of molecular junctions. *Science* **301**, 1221-1223 (2003).
15. Venkataraman, L., Klare, J. E., Nuckolls, C., Hybertsen, M. S. & Steigerwald, M. L. Dependence of single-molecule junction conductance on molecular conformation. *Nature* **442**, 904-907 (2006).
16. Aradhya, S. V. *et al.* Dissecting contact mechanics from quantum interference in single-molecule junctions of stilbene derivatives. *Nano Lett.* **12**, 1643-1647 (2012).
17. Hong, W. *et al.* Single molecular conductance of tolanes: experimental and theoretical study on the junction evolution dependent on the anchoring group. *J. Am. Chem. Soc.* **134**, 2292-2304 (2012).
18. Lovat, G. *et al.* Room-temperature current blockade in atomically defined single-cluster junctions. *Nat. Nanotechnol.* **12**, 1050-1054 (2017).
19. Guo, S., Hihath, J., Díez-Pérez, I. & Tao, N. Measurement and Statistical Analysis of Single-Molecule Current–Voltage Characteristics, Transition Voltage Spectroscopy, and Tunneling Barrier Height. *J. Am. Chem. Soc.* **133**, 19189-19197 (2011).
20. Huisman, E. H., Guédon, C. M., van Wees, B. J. & van der Molen, S. J. Interpretation of Transition Voltage Spectroscopy. *Nano Lett.* **9**, 3909-3913 (2009).
21. Gu, J. & Leszczynski, J. A DFT Study of the Water-Assisted Intramolecular Proton Transfer in the Tautomers of Adenine. *J. Chem. Phys. A* **103**, 2744-2750 (1999).
22. Markova, N., Enchev, V. & Timtcheva, I. Oxo–Hydroxy Tautomerism of 5-Fluorouracil: Water-Assisted Proton Transfer. *J. Chem. Phys. A* **109**, 1981-1988 (2005).
23. Huang, X. *et al.* Electric field-induced selective catalysis of single-molecule reaction. *Sci. Adv.* **5**, eaaw3072 (2019).
24. Gilat, S. L., Kawai, S. H. & Lehn, J.-M. Light-Triggered Molecular Devices: Photochemical Switching Of optical and Electrochemical Properties in Molecular Wire Type Diarylethene Species. *Chem. Eur. J.* **1**, 275-284 (1995).
25. Lara-Avila, S. *et al.* Light-Triggered Conductance Switching in Single-Molecule Dihydroazulene/Vinylheptafulvene Junctions. *J. Phys. Chem. C* **115**, 18372-18377 (2011).
26. Sun, L. *et al.* Single-molecule electronics: from chemical design to functional devices. *Chem. Soc. Rev.* **43**, 7378-7411 (2014).
27. Turecek, F., Brabec, L. & Korvola, J. Unstable enols in the gas phase. Preparation ionization, energies, and heats of formation of (E)-and (Z)-2-buten-2-ol, 2-methyl-1-propen-1-ol, and 3-methyl-2-buten-2-ol.

J. Am. Chem. Soc. **110**, 7984-7990 (1988).

28. Rappoport, Z. *Chemistry of enols*. (J. Wiley, 1990).
29. Bednarek, P. *et al.* Electron-Transfer-Induced Tautomerization in Methylindanones: Electronic Control of the Tunneling Rate for Enolization. *J. Am. Chem. Soc.* **123**, 2377-2387 (2001).
30. Bally, T. Electron-Transfer-Induced Tautomerizations. *Tautomerism: Concepts and Applications in Science and Technology*, 75-94 (2016).
31. Marcus, R. A. & Sutin, N. Electron transfers in chemistry and biology. *Biochimica et Biophysica Acta (BBA) - Reviews on Bioenergetics* **811**, 265-322 (1985).
32. Sowa, J. K., Mol, J. A., Briggs, G. A. D. & Gauger, E. M. Beyond Marcus theory and the Landauer-Büttiker approach in molecular junctions: A unified framework. *J. Chem. Phys.* **149**, 154112 (2018).
33. Migliore, A., Schiff, P. & Nitzan, A. On the relationship between molecular state and single electron pictures in simple electrochemical junctions. *Phys. Chem. Chem. Phys.* **14**, 13746-13753 (2012).
34. Tang, C. *et al.* Multicenter-Bond-Based Quantum Interference in Charge Transport Through Single-Molecule Carborane Junctions. *Angew. Chem. Int. Ed.* **58**, 10601-10605 (2019).
35. Chen, Z. *et al.* Modularized Tuning of Charge Transport through Highly Twisted and Localized Single-Molecule Junctions. *J. Phys. Chem. Lett.* **10**, 3453-3458 (2019).
36. Capozzi, B. *et al.* Single-molecule diodes with high rectification ratios through environmental control. *Nat. Nanotechnol.* **10**, 522-527 (2015).
37. Lin, L. *et al.* Spectral Clustering to Analyse the hidden Events in Single-Molecule Break Junctions. *Submitted*.
38. Frisch, M. *et al.* (Gaussian, Inc., Wallingford CT, 2013).
39. Shaik, S., Ramanan, R., Danovich, D. & Mandal, D. Structure and reactivity/selectivity control by oriented-external electric fields. *Chem. Soc. Rev.* **47**, 5125-5145 (2018).
40. Stuyver, T., Danovich, D., Joy, J. & Shaik, S. External electric field effects on chemical structure and reactivity. *WIREs Computational Molecular Science* **10**, e1438 (2020).
41. Dutta Dubey, K., Stuyver, T., Kalita, S. & Shaik, S. Solvent Organization and Rate Regulation of a Menshutkin Reaction by Oriented External Electric Fields are Revealed by Combined MD and QM/MM Calculations. *J. Am. Chem. Soc.* **142**, 9955-9965 (2020).
42. Deffner, M. *et al.* (Universität Hamburg, 2010).
43. Garner, M. H. *et al.* Comprehensive suppression of single-molecule conductance using destructive σ-interference. *Nature* **558**, 415-419 (2018).
44. Garner, M. H. *et al.* Permethylation Introduces Destructive Quantum Interference in Saturated Silanes. *J. Am. Chem. Soc.* **141**, 15471-15476 (2019).
45. Herrmann, C., Solomon, G. C., Subotnik, J. E., Mujica, V. & Ratner, M. A. Ghost transmission: How large basis sets can make electron transport calculations worse. *J. Chem. Phys.* **132**, 024103 (2010).
46. Herrmann, C., Solomon, G. C. & Ratner, M. A. Designing organic spin filters in the coherent tunneling regime. *J. Chem. Phys.* **134**, 224306 (2011).

Figures

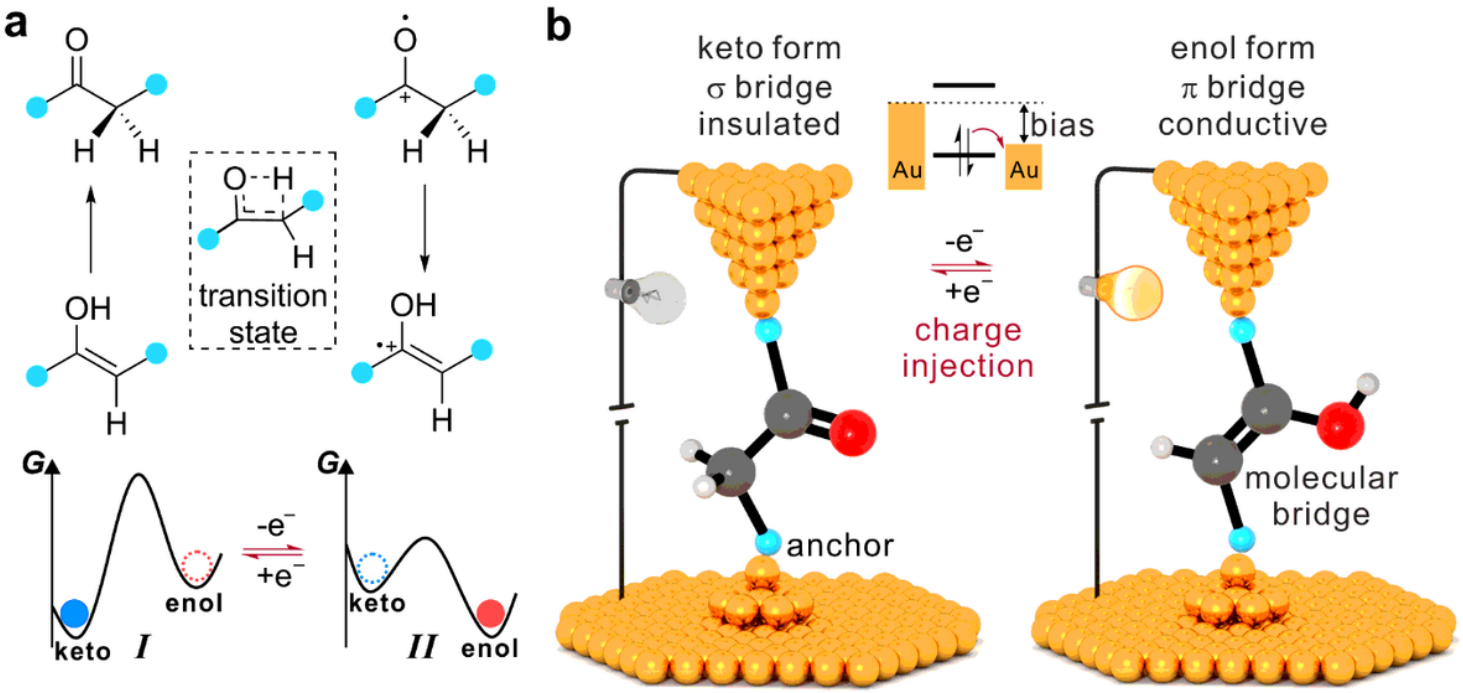

Figure 1

Schematic diagram of the tautomerization based single-molecule switch. a, Reaction scheme of the keto-enol tautomerization via its four-membered transition state. The sketched PESs I and II are correspondingly shown. The four-membered transition state is shown inside the dotted box. b, Schematic representation of the STM-BJ setup and the tautomerization-based switch. The switch is in the low-conductance keto state in which a bridge connects the two contacts (left). The charge injection leads to the switching to the high-conductance state with a bridge connecting the two electrodes (right). The sketched energy diagram of the charge injection is shown in the middle. The blue balls represent anchor groups. The grey, red, and white balls represent carbon, oxygen, and hydrogen, respectively.

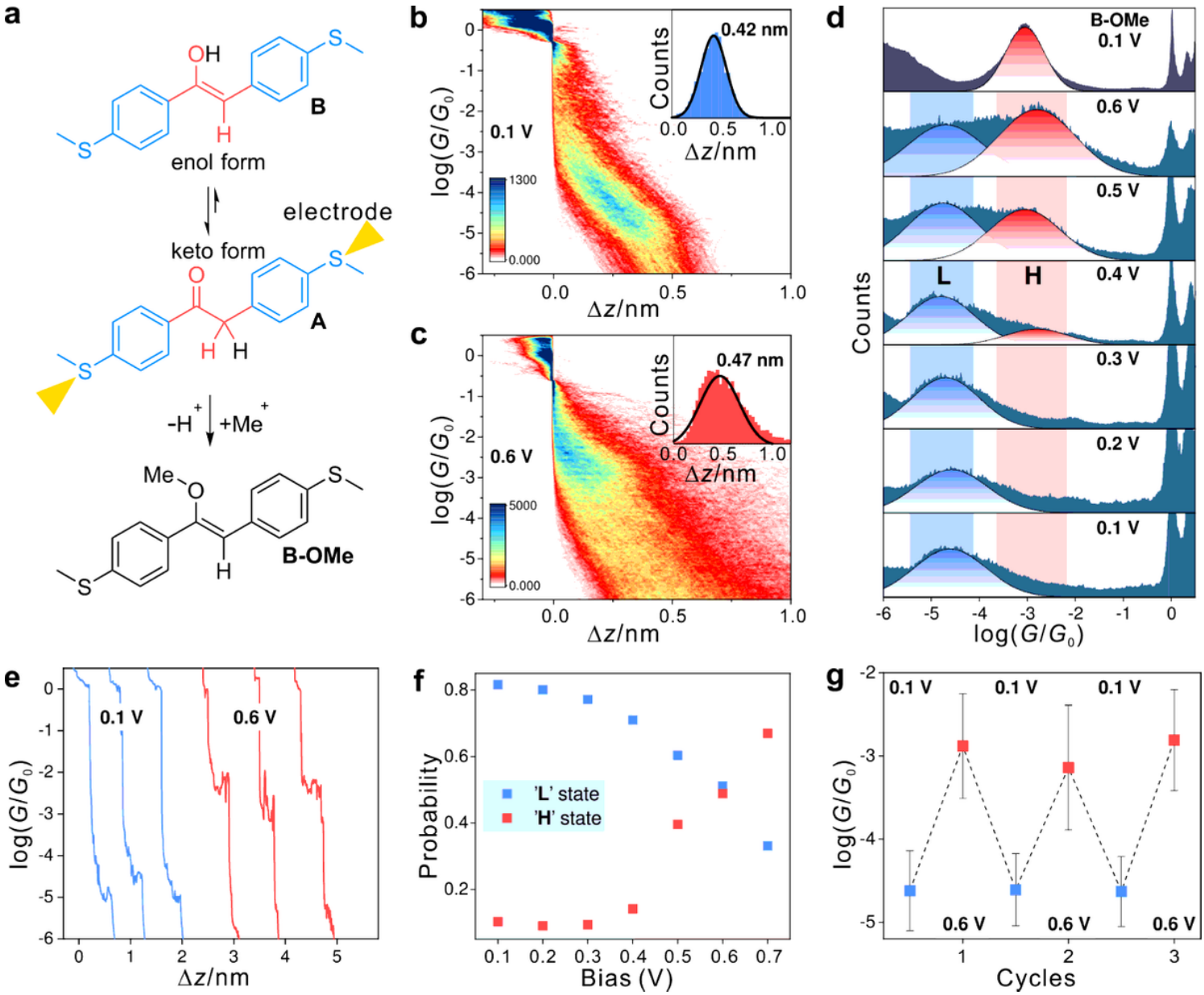

Figure 2

Single-molecule conductance characterization. a, Chemical structure of A, which is formally in a tautomeric equilibrium with its enol isomer B. The keto form dominates this equilibrium. B-OMe, the methylated analogue of enol form B, is formed by methylation of A. b,c, 2D conductance histograms of A at 0.1 (b) and 0.6 V (c) bias, with the corresponding stretching distances shown in the inset. d, 1D conductance histograms of A characterized at different biases ranging from 0.1 to 0.6 V. The low and high-conductance states are labeled 'L' and 'H', respectively. The 1D conductance histogram of B-OMe in 0.1 V bias is shown on the upper side. e, Typical individual conductance traces of A characterized at 0.1 V (blue lines) and 0.6 V (red lines) biases. f, Distribution probabilities of states 'L' and 'H' plotted against different biases. g, Peak centers of the dominant conductance peaks of the corresponding 1D conductance histograms with alternation of the bias between 0.1 and 0.6 V. The error was defined as the standard deviation of the Gaussian fitting.

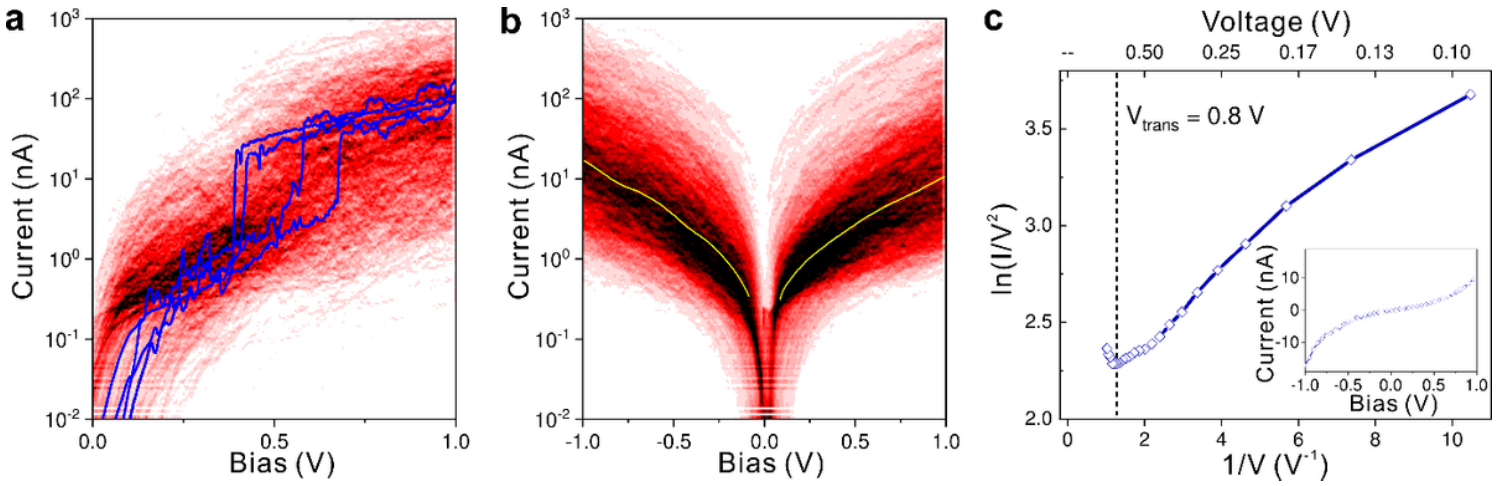

Figure 3

I-V characterization. a, 2D I-V histogram of the switching traces is constructed from 831 traces. Four representative I-V curves showing the switching from a low-conductance state to a high-conductance state are plotted in blue. b, 2D I-V histogram constructed from 2542 traces. The yellow line was achieved by the Gaussian fitting in each row of bins. c, Transition voltage spectrum constructed from the above-fitted line. The inset shows the fitted line on a linear scale.

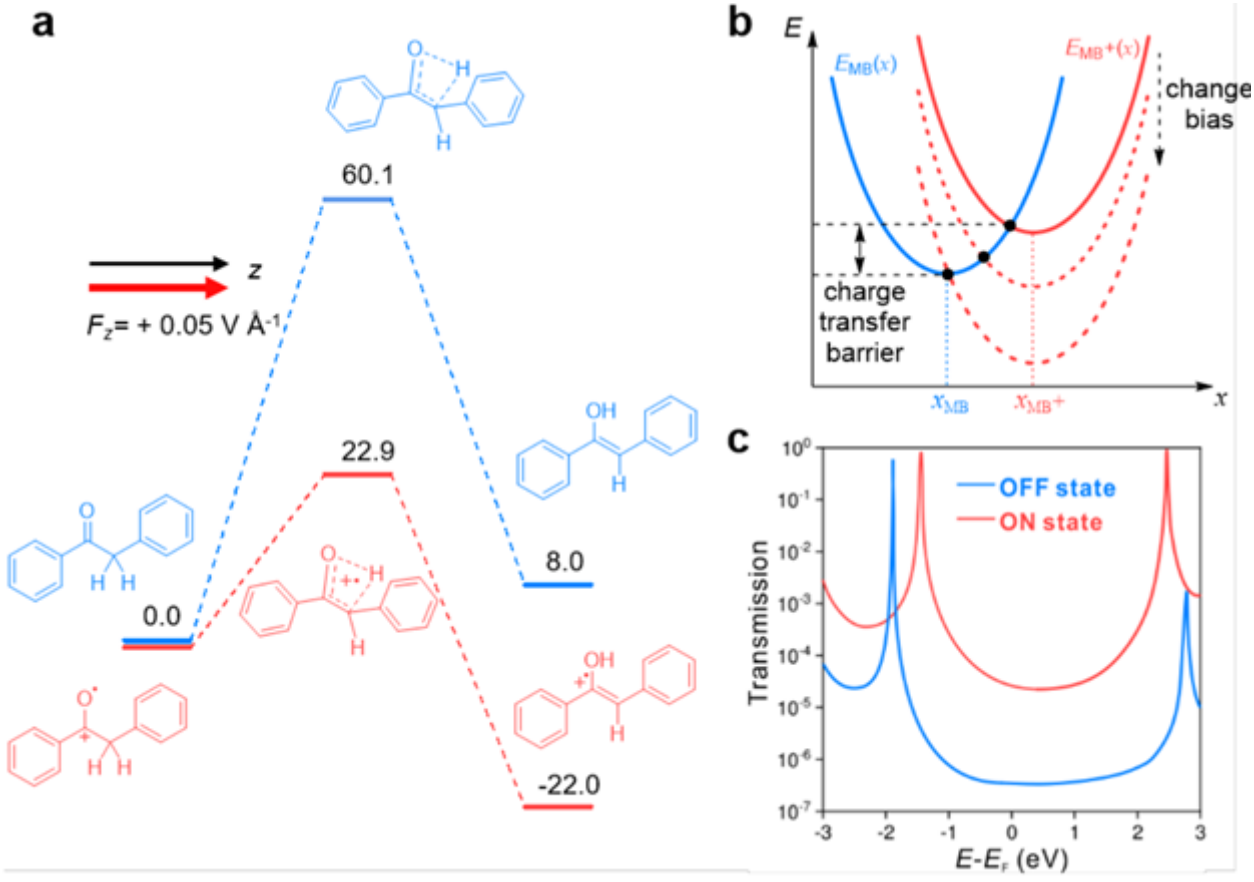

Figure 4

Calculated reaction profile and transmission coefficient. a, Reaction profile (in kcal mol-1) associated with the tautomerization reaction on the ground-state, i.e., uncharged, PES (blue), and on the PES of the radical, cationic species obtained after charge injection (red), calculated at B3LYP/def2-TZVP level of theory. An electric field corresponding to the field exerted by the approximate threshold voltage in the junction has been included (the effect of a reversal of the field direction on the profile is shown in the Extended Data Fig. 8). b, Schematic representation of the Marcus parabolas, describing the system free energy as a function of the environmental dielectric coordinate x, for the uncharged MB species (parabola in blue centered around xMB) and the charged MB (MB+) species (parabola in red centered around xMB+). As the molecule-metal potential difference changes, the MB+-parabola shifts vertically. c, Calculated transmission spectra of the ON and OFF states.

Supplementary Files

This is a list of supplementary files associated with this preprint. Click to download.

- SupportingInformation.docx
- FigS1.png
- floatimage6.jpeg
- floatimage7.jpeg
- Onlinefloatimage8.Png
- Onlinefloatimage9.Png
- Onlinefloatimage10.Png
- Onlinefloatimage11.Png
- Onlinefloatimage12.Png
- Onlinefloatimage13.Png